

# **Turbulence Measurements from Compliant Moorings - Part II: Motion**

## **Correction**

Levi F. Kilcher\*

*National Renewable Energy Laboratory, Golden, Colorado, USA*

Jim Thomson

*Applied Physics Laboratory, University of Washington, Seattle, Washington, USA*

Samuel Harding

*Pacific Northwest National Laboratory, Richland, Washington, USA*

Sven Nylund

*Nortek AS, Norway*

\* *Corresponding author address:* Levi Kilcher, National Renewable Energy Laboratory, 15013 Denver West Pkwy, Golden, Colorado, USA

E-mail: Levi.Kilcher@nrel.gov

## ABSTRACT

14 Acoustic Doppler velocimeters (ADV) are a valuable tool for making  
15 high-precision measurements of turbulence, and moorings are a convenient  
16 and ubiquitous platform for making many kinds of measurements in the  
17 ocean. However, because of concerns that mooring motion can contami-  
18 nate turbulence measurements and acoustic Doppler profilers are relatively  
19 easy to deploy, ADVs are not frequently deployed from moorings. This  
20 work demonstrates that inertial motion measurements can be used to reduce  
21 motion-contamination from moored ADV velocity measurements. Three dis-  
22 tinct mooring platforms were deployed in a tidal channel with inertial-motion-  
23 sensor-equipped ADVs. In each case, the motion correction based on the in-  
24 ertial measurements dramatically reduced contamination from mooring mo-  
25 tion. The spectra from these measurements have a shape that is consistent  
26 with other measurements in tidal channels, and have a  $f^{-5/3}$  slope at high  
27 frequencies—consistent with Kolmogorov’s theory of isotropic turbulence.  
28 Motion correction also improves estimates of cross spectra and Reynold’s  
29 stresses. Comparison of turbulence dissipation with flow speed and turbu-  
30 lence production indicates a bottom boundary layer production-dissipation  
31 balance during ebb and flood that is consistent with the strong tidal forcing  
32 at the site. These results indicate that inertial-motion-sensor-equipped ADVs  
33 are a valuable new tool for measuring turbulence from moorings.

## 34 1. Introduction

35 Acoustic Doppler velocimeters (ADV) have been used to make high-precision measurements of  
36 water velocity for over 20 years (Kraus et al. 1994; Lohrmann et al. 1995). During that time, they  
37 have been deployed around the world to measure turbulence from a range of platforms, including  
38 the laboratory setting (Voulgaris and Trowbridge 1998), from stationary structures on ocean-, river-  
39 and lake-bottoms (Kim et al. 2000; Lorke 2007; Cartwright et al. 2009), in surface waters from  
40 a pole lowered from a ship’s bow (Geyer et al. 2008), and in the deep ocean from autonomous  
41 underwater vehicles (e.g., Zhang et al. 2001; Goodman et al. 2006).

42 A relatively small fraction of ADV measurements have been made from moorings (e.g., Fer  
43 and Paskyabi 2014). Presumably this is because mooring motion can contaminate ADV mea-  
44 surements, and acoustic Doppler profilers (ADPs) can be used to measure mid-depth turbulence  
45 statistics without a mooring (e.g., Stacey et al. 1999a; Rippeth et al. 2002; Wiles et al. 2006).  
46 Still, ADV measurements have distinct characteristics that can be advantageous: they are capa-  
47 ble of higher sample rates, have higher signal-to-noise ratios, and have a much smaller sample  
48 volume (1 centimeter, as opposed to several meters). That is, compared to an ADP, ADVs are  
49 high-precision instruments capable of providing unique information. They could be more widely  
50 used as a moored instrument (i.e., at an arbitrary depth) if a method for accounting for mooring  
51 motion can be demonstrated to provide more accurate estimates of turbulence statistics.

52 Inertial motion unit (IMU) sensors have been used in the aerospace and aeronautical industries  
53 to quantify the motion of a wide range of systems, and to improve atmospheric velocity measure-  
54 ments, for several decades (Axford 1968; Edson et al. 1998; Bevly 2004). Over the last 10 years,  
55 the smartphone, drone, and ‘Internet of Things’ markets have driven innovation in microelectrical-  
56 mechanical systems, including the IMU. As a result of this growth and innovation, the cost, power

57 requirements, and size of IMUs have come down. These changes have allowed these sensors to be  
58 integrated into oceanographic instruments that have small form-factors, and rely on battery power.

59 Nortek now offers a version of their Vector ADV with a Microstrain 3DM-GX3-25 IMU sensor  
60 (Nortek 2005; MicroStrain 2012). This IMU's signals are incorporated into the Vector data stream,  
61 so that its motion and orientation signals are tightly synchronized with the ADV's velocity mea-  
62 surements. This tight synchronization provides a data stream that can be utilized to quantify ADV  
63 motion in the Earth's inertial reference frame, and remove that motion from the ADV's velocity  
64 measurements at each time step of its sampling (Edson et al. 1998). This work utilizes moored  
65 'ADV-IMU' measurements from mid-depths in Puget Sound to demonstrate that motion correc-  
66 tion can improve the accuracy of oceanic turbulence spectra, turbulence dissipation, and Reynolds  
67 stress estimates from moored platforms.

68 This effort was originally motivated by a need for low-cost, high-precision turbulence measure-  
69 ments for the emerging tidal energy industry (McCaffrey et al. 2015; Alexander and Hamlington  
70 2015). Experience in the wind energy industry has shown that wind turbine lifetime is reduced  
71 by atmospheric turbulence, and the same is expected to be true for tidal energy turbines. In the  
72 atmosphere, meteorological towers are often used to position sonic anemometers at the hub height  
73 of wind turbines for measuring detailed turbulence inflow statistics (Hand et al. 2003; Kelley et al.  
74 2005; Mücke et al. 2011; Afgan et al. 2013). In the ocean, tower-mounted hub-height turbulence  
75 measurements have been made, but they are challenging to install and maintain in energetic tidal  
76 sites (Gunawan et al. 2014; Thomson et al. 2012). Therefore, the U.S. Department of Energy  
77 funded this work to investigate the accuracy of mooring-deployed ADV-IMUs to reduce the cost  
78 of turbulence measurements at tidal energy sites (Kilcher et al. 2016). The approach proved to be  
79 successful and potentially useful to the broader oceanographic community interested in moored

80 turbulence measurements (Lueck and Huang 1999; Doherty et al. 1999; Nash et al. 2004; Perlin  
81 and Moum 2012; Alford 2010; Paskyabi and Fer 2013).

82 The next section describes details of the measurements, including a summary of the hardware  
83 configurations (platforms) that were used to support and position the ADV-IMUs in the water  
84 column. A detailed description of the motion of these platforms is found in the companion paper to  
85 this work, Harding et al. (in review), hereafter Part 1. Section 3 describes the mathematical details  
86 of motion correction and Section 4 presents results from applying the method to measurements  
87 from the various platforms. Section 5 is a discussion of the energetics of the tidal channel in  
88 which the measurements were made and demonstrates that the measurements are consistent with  
89 turbulence theory and other measurements in similar regimes. A summary and concluding remarks  
90 are provided in Section 6.

## 91 **2. Measurements**

92 This work focuses on measuring turbulence from ADVs that are equipped with IMUs and de-  
93 ployed from moving (moored) platforms. The ADVs utilized for these measurements were Nortek  
94 Vector ADVs equipped with Microstrain 3DM-GX3-25 IMU sensors. These IMUs captured all  
95 six components of the ADV motion (three components of angular rotation and three components  
96 of linear acceleration), as well as the orientation of the ADV pressure case. The sampling of the  
97 motion sensor is tightly synchronized with the ADV measurements. The IMU measures its mo-  
98 tion at 1 kHz and uses internal signal integration (Kalman filtering) to output the motion signals  
99 at the same sample rate as the ADV's velocity measurements. This reduces aliasing of the IMU's  
100 motion measurements above the ADV's sample rate (MicroStrain 2010). Cable-head ADVs were  
101 used throughout this work to allow for flexibility in the positioning of the ADV head relative to its  
102 pressure case.

103 All measurements used in this work were made in Admiralty Inlet, Washington, approximately  
104 500 m west southwest of Admiralty Head in 60 m of water near 48° 9.18' N, 122° 41.22' W (Figure  
105 1). The site is approximately 6 km east of Port Townsend, and 1 km north of the Port Townsend  
106 to Coupeville ferry route. Admiralty inlet is the largest waterway connecting Puget Sound to  
107 the Strait of Juan de Fuca, and it possesses a large semidiurnal tidal flow (Thomson et al. 2012;  
108 Polagye and Thomson 2013). This work utilizes data from three distinct deployment platforms:  
109 the tidal turbulence mooring, a StableMoor buoy, and a simple sounding weight. All data used  
110 in this analysis are available from the MHK data repository (<http://mhkdr.openei.org>; submission  
111 ids: 49, 50 and 51). Each of these platforms are briefly described below, and additional details,  
112 photos, and schematic diagrams can be found in Part 1.

### 113 *a. Tidal Turbulence Mooring*

114 The tidal turbulence mooring (TTM) is a simple mooring system with a strongback fin sus-  
115 pended between a steel clump-weight anchor weighing 1,200 kg when dry and a 0.93-m-diameter  
116 spherical steel buoy with a buoyancy of 320 kg. The ADV pressure cases were clamped to one  
117 side of the strongback fin and the ADV sensor head was positioned 10 cm in front of the fin's  
118 leading edge (Figure 2). The leading edge of the fin is fastened inline with the mooring line. This  
119 configuration was designed to work like a weather vane, such that the drag on the fin held the ADV  
120 head upstream of the mooring components. This work utilizes data from two TTM deployments.

121 The first TTM deployment was in June 2012 from 17:30 on the 12th until 14:30 on the 14th  
122 (local; i.e., Pacific Daylight Time). Two Nortek ADVs were clamped to either side of the fin so that  
123 the axis of their cylindrical pressure cases were parallel with the leading edge of the strongback.  
124 The ADV heads were spaced 0.5 m apart vertically along the fin. Only one of these ADVs was

125 equipped with an integrated IMU. This TTM also had an upward-looking acoustic Doppler profiler  
126 mounted on the mooring anchor.

127 Periods of time during which this mooring interfered with a beam of the Doppler profiler were  
128 identified by inspecting the profiler's acoustic amplitude signal. Periods during which one beam  
129 of the profiler had  $> 5\%$  higher acoustic amplitude than the other beams were flagged as "contam-  
130 inated" and excluded from averaging. Five-minute averages in which more than 50% of the data  
131 were contaminated in this way were masked as invalid.

132 The second TTM deployment was in 2014 from 06:00 on June 17 to 05:00 on June 19 (local  
133 time). Two Nortek ADV-IMUs were mounted on this TTM, with their heads spaced 0.5 m apart  
134 along the fin. In this case, the pressure cases and ADV heads were inclined at an angle of  $18^\circ$  to  
135 the leading edge of the fin to account for mooring blowdown during strong currents (Figure 3).  
136 This change was made to reduce vibrational motion observed during the June 2012 deployment  
137 that was believed to be associated with the orientation of the pressure cases.

#### 138 *b. The StableMoor platform*

139 The second deployment platform was a cylindrical, StableMoor, syntactic foam buoy (manufac-  
140 turer: Deep Water Buoyancy) that was anchored to a clump weight that weighed 1,200 kg (Figure  
141 4). The buoy is 3.5 m long and 0.45 m in diameter with a tail ring that is 0.76 m in diameter. The  
142 StableMoor buoy weighs 295 kg in air, and has a buoyancy of 185 kg in water.

143 The StableMoor buoy was deployed with an ADV-IMU mounted at its nose from 11:21 on May  
144 12 to 11:53 on May 13, 2015 (local time). The sample volume of the ADV is 10 cm forward of  
145 the nose and 20 cm above the center line of the StableMoor buoy (Figure 4). Based on Wyngaard  
146 et al.'s (1985) investigation of a similarly shaped slender body, the velocity measurements should  
147 have flow-distortion effects of less than 10%. This configuration was designed to be the most

148 stable platform for measuring turbulence from a moving platform. The StableMoor buoy was  
149 equipped with a 1,200-kHz RDI workhorse sentinel acoustic Doppler profiler that was oriented  
150 downward-looking to measure water velocity below the platform in twelve 1-m bins and measure  
151 buoy motion (“bottom tracking”), all at a 1-Hz sample rate.

152 The buoy was ballasted to pitch upward a few degrees in zero-flow to avoid “flying downward”.  
153 In the presence of an oncoming current, the tail fins help to orient it into the flow. The anchor for  
154 this buoy is similar to that of the TTM, including an acoustic release so the mooring and anchor  
155 can be recovered separately.

156 The StableMoor platform has two primary advantages compared to the TTM. First, it is signif-  
157 icantly more massive and hydrodynamically stable than the TTM, which reduces the frequency  
158 of motions of the platform. Second, the StableMoor platform is capable of supporting a bottom-  
159 tracking acoustic Doppler profiler, which provides an independent measure of the platform’s trans-  
160 lational motion. Disadvantages of the StableMoor include: its size, which adds to the challenge of  
161 deployment and recovery, and its cost, which is significantly higher than the TTM system.

### 162 *c. Turbulence Torpedo*

163 The turbulence torpedo is a simple sounding weight with an ADV head mounted forward of the  
164 nose, and the ADV pressure case strapped below (Figure 5). This platform was deployed on May  
165 14, 2015, for 37 minutes starting at 07:41 local time. This measurement was made from a davit  
166 that hung the system from the side of the ship to a depth of approximately 25 m. The primary  
167 logistical advantages of this platform are its compact size, low cost, and the flexibility to perform  
168 spatial transects.



169 *d. Coordinate system and turbulence averaging*

170 Unless stated otherwise, vector quantities in this work are in a fixed “principal-axes” coordinate  
 171 system that is aligned with the bidirectional tidal flow: positive  $u$  is in the direction of ebb (310°  
 172 True), positive  $w$  is vertically upward, and  $v$  is the cross-stream component in a right-handed  
 173 coordinate system. The full velocity vector,  $\vec{u} = (\tilde{u}, \tilde{v}, \tilde{w})$ , is separated into a mean and turbulent  
 174 component as  $\vec{u} = \overline{\vec{u}} + \vec{u}'$ , where the over-bar denotes a 5-minute average. Turbulence kinetic  
 175 energy,  $\text{tke} = \overline{u'^2} + \overline{v'^2} + \overline{w'^2}$ , and Reynold’s stresses,  $\overline{uv}$ ,  $\overline{uw}$ ,  $\overline{vw}$ , are computed by averaging over the  
 176 5-minute window. Throughout this work, we use  $\bar{U} = (\bar{u}^2 + \bar{v}^2)^{1/2}$  to denote the mean horizontal  
 177 velocity magnitude.

178 All spectra,  $S\{x\}(f) = |\mathcal{F}\{x(t)\}|^2$ , and cross spectra,  $C\{x, y\}(f) = \text{real}(\mathcal{F}\{x(t)\}\mathcal{F}\{y(t)\})$ , are  
 179 computed using NumPy fast Fourier transform routines (van der Walt et al. 2011). Here,  $\mathcal{F}\{x(t)\}$   
 180 denotes the fast Fourier transform of a signal  $x(t)$ . Time series, e.g.,  $x(t)$ , are linearly detrended  
 181 and Hanning windowed prior to computing  $\mathcal{F}\{x\}$  to reduce spectral reddening.

182 Throughout the remainder of this work, the dependence of  $S$  and  $C$  on  $f$  is implied (e.g.,  $S\{x\}(f)$   
 183 is hereafter  $S\{x\}$ ), and for other variables the dependence on  $t$  is implied. Spectra and cross  
 184 spectra are normalized to preserve variance:  $\int S\{u\}df = \overline{u^2}$ , and  $\int C\{u, v\}df = \overline{uv}$ . The notations  
 185  $S\{\vec{u}\} = (S\{u\}, S\{v\}, S\{w\})$ , and  $C\{\vec{u}\} = (C\{u, v\}, C\{u, w\}, C\{v, w\})$  denote the set of spectra and  
 186 cross spectra for each velocity component and pairs of components, respectively.

187 Turbulence dissipation rates are computed as:

$$\varepsilon = \frac{1}{\bar{U}} \left( \alpha \left\langle (S\{u\} + S\{v\} + S\{w\}) f^{5/3} \right\rangle_{f_{IS}} \right)^{3/2} \quad (1)$$

188 where  $\alpha = 0.5$  and  $\langle \rangle_{f_{IS}}$  denotes an average over the inertial subrange of the velocity spectra and  
 189 where the signal-to-noise ratio is small (Lumley and Terray 1983; Sreenivasan 1995). Throughout

this work, we take this average from 0.3 to 1 Hz for the  $u$  and  $v$  components, and 0.3 to 3 Hz for the  $w$  component.

### 3. Methodology

This work describes a method for correcting velocity measurements from a moving velocity sensor,  $\vec{u}_m$ , using independent measurements of that sensor's motion,  $\vec{u}_h$ , to remove the motion from the velocity measurements, and thus estimate the ‘motion corrected velocity’:

$$\vec{u}(t) = \vec{u}_m(t) + \vec{u}_h(t) \quad . \quad (2)$$

Note here that the ‘+’-sign is correct because head motion,  $\vec{u}_h$ , induces a measured velocity in the opposite direction of the head motion itself ( $\vec{u}_m = \vec{u} - \vec{u}_h$ ). This approach has been used to successfully correct sonic anemometer measurements of atmospheric turbulence (e.g., Edson et al. 1998; Miller et al. 2008). In the ocean, previous works have utilized inertial motion sensors to quantify the motion of multiscale profilers for the purpose of measuring the full spectrum of oceanic shear (Winkel et al. 1996), and to quantify the motion of thermistor sensors (Moum and Nash 2009), but the Edson et al. (1998) approach has not been documented for moored ADV measurements.

The Microstrain IMU available in the Nortek Vector ADV measures the linear acceleration,  $\vec{a}$ , rotational motion,  $\vec{\omega}$ , and orientation matrix,  $\mathbf{R}$ , of the ADV pressure case in the Earth reference frame at every time step of the ADV's sampling. So long as the ADV head is rigidly connected to the IMU (i.e. the ADV pressure case), the motion of the ADV head is calculated from these signals as the sum of rotational and translational motion:

$$\begin{aligned} \vec{u}_h &= \vec{u}_\omega + \vec{u}_a + \vec{u}_{\text{low}} \\ &= \mathbf{R}^T \cdot \vec{\omega}^*(t) \times \vec{\ell}^* + \int \{\vec{a}(t)\}_{HP(f_a)} dt + \vec{u}_{\text{low}} \end{aligned} \quad (3)$$

Here, \* superscripts denote quantities in the ADV's local coordinate system, and  $\vec{\ell}^*$  is the vector from the IMU to the ADV head.  $\mathbf{R}^T$ —the inverse of the orientation matrix—rotates vectors from the IMU to the Earth reference frame. The notation  $\{\vec{a}\}_{HP(f_a)}$  indicates that the IMU's accelerometer signal is high-pass filtered (in the Earth's stationary reference frame) at a chosen filter frequency,  $f_a$ . Without such filtering, low-frequency noise in  $\vec{a}$ —sometimes referred to as bias drift—is amplified by integration to the point that it overwhelms the higher frequency information (Barshan and Durrant-Whyte 1995; Bevy 2004; Gulmammadov 2009).  $\vec{u}_{\text{low}}$  is the low-frequency translational motion that is unresolved by  $\vec{u}_a$ , and it is discussed in more detail below. Note that, to avoid double counting,  $\vec{u}_{\text{low}}$  should be estimated by applying the complementary low-pass filter to the independent measurement of low-frequency motion. We use fourth order, zero-phase (bidirectional), Hanning filters for all filtering operations.

The noise levels of the IMU,  $\vec{n}_\omega$  and  $\vec{n}_a$ , are computed from ADV-IMU data collected while the instrument was resting motionless on a table for several hours. Where, for this motionless dataset, the noise levels are defined according to (3) with  $\vec{n}_\omega$  in place of  $\vec{u}_\omega$ , and  $\vec{n}_a$  in place of  $\vec{u}_a$ . These are presented in Figure 6 relative to the ADV spectra presented in following sections of this paper (grey shading), and relative to the Doppler noise levels of the ADV.

$S\{\vec{n}_\omega\}$  is equal in all three components, and so only one component is presented for simplicity (yellow).  $S\{\vec{n}_\omega\}$  is several orders of magnitude lower than the velocity spectra we measured (grey region), and also more than an order of magnitude smaller than the Doppler noise levels of the ADV. Here we have used  $\vec{\ell}^* = 1$  m; which is the order-of-magnitude of the typical distance between the ADV head and the IMU. This indicates that the precision of  $\vec{u}_\omega$  (i.e. the angular rate sensor) is adequate for making corrections to ADV velocity measurements without filtering.

The noise level of  $S\{\vec{u}_a\}$  (Figure 6, black), on the other hand, is dominated by a  $f^{-2}$  slope that results from integrating the low-frequency noise in  $\vec{a}$ . The horizontal ( $u$  and  $v$ ) spectra of

these noise levels are identical, and so we only present one of them for simplicity (solid lines). The vertical spectra noise levels are different because the signal-to-noise ratio is larger (dashed black lines). High-pass filtering reduces the low-frequency noise (purple and green) so that it does not contaminate motion correction, but any real motion that does exist at these frequencies is lost (Egeland 2014; VanZwieten et al. 2015). This means there is a residual low-frequency translational motion,  $\vec{u}_{\text{low}}$ , that needs to be measured independently—or at the very least considered—when using ADV-IMU data from moving platforms.

For the StableMoor buoy, the ADP bottom-track measured  $\vec{u}_{\text{low}}$ , and this measurement agrees with  $\vec{u}_a$  over a narrow frequency band (see Part I, appendix A), indicating that the ADP and IMU are resolving the same motion. Furthermore,  $\vec{u}_{\text{low}}$  derived from the ADP bottom-track gives a noteworthy improvement in the shape of  $S\{u\}$  and  $S\{v\}$  when compared to similar spectra that assume  $\vec{u}_{\text{low}} = 0$ . In the latter case, spectral peaks and dips are present between 0.01 and 0.1 Hz that are inconsistent with other measurements of oceanic turbulence (not shown). This indicates that ADP bottom-track measurements are important for resolving turbulence spectra from the StableMoor buoy platform. For the StableMoor buoy we utilize  $f_a = 0.2\text{Hz}$  (5-s period); further details of this choice can be found in appendix A of Part I.

For the TTM the ADV position, relative to its base, can be estimated by assuming the mooring acts like a rigid pole and using the IMU orientation matrix to estimate the pole’s ‘lean’. The position obtained from this model can then be differentiated to estimate  $\vec{u}_{\text{low}}$  (this model does not apply at high frequencies). Spectra of  $\vec{u}_{\text{low}}$  estimated using this approach for the June 2014 TTM deployment (Figure 6, blue) are plotted up to the point where they cross their respective  $S\{\vec{u}_a\}$  noise level (black). Together, these two lines provide an ‘aggregate noise level’ of translational velocity estimates for the TTM: the rigid pole estimate of  $\vec{u}_{\text{low}}$  indicates the amplitude of unresolved motion at low- $f$  (blue), and  $S\{\vec{u}_a\}$  indicates the limits of the IMU at high- $f$  (black).

257 Coincidentally,  $S\{\vec{u}_a\}$  filtered at  $f_a = 0.0333\text{Hz}$  is not a terrible approximation for this aggregate  
258 noise level. Furthermore, because this aggregate noise level is more than an order of magnitude  
259 lower than the velocity spectra of interest (shaded region), the results of motion correction are  
260 essentially identical whether we use the rigid pole model to estimate  $\vec{u}_{\text{low}}$ , or if we simply assume  
261 that  $\vec{u}_{\text{low}} = 0$ . Either way, we use  $f_a = 0.0333\text{Hz}$  (30-s period) for the TTM.

262 The choice of  $f_a$  for reducing low-frequency accelerometer noise depends on the application of  
263 the measurement and the platform being used. In particular, filter selection involves a trade-off  
264 between filtering out the bias drift noise while not filtering out measured motion that is unresolved  
265 by an independent measurement of  $\vec{u}_{\text{low}}$ . In the course of this work we tried several different  
266 filter frequencies (from 0.2 to 0.00333 Hz; i.e. 5 second to 5 minute periods). The results of this  
267 comparison are presented in the supplementary material. In general, we recommend selecting the  
268 highest-frequency for  $f_a$  that does not result in statistically significant changes in motion corrected  
269 velocity spectral shape compared to a lower value of  $f_a$ . This is likely to depend on the dynamics  
270 of the platform used to support the ADV, and the intensity of the turbulence being measured.  
271 Ultimately, without an independent estimate of  $\vec{u}_{\text{low}}$ , one should use caution when utilizing the  
272 portion of the motion-corrected velocity spectrum below  $f_a$ .

273 Additional details on motion correction—including a detailed accounting of the distinct co-  
274 ordinate systems of the IMU, ADV pressure case, and ADV head—can be found in Kilcher  
275 et al. (2016). Open-source Python tools for performing motion correction of ADV-IMU data—  
276 including scripts that write processed data in Matlab and tabulated formats—are available at  
277 <http://lkilcher.github.io/dolfyn/>.

## 4. Results

### *a. Mean velocity*

Figure 7 shows a comparison of  $\vec{u}$  measured by an ADV-IMU mounted on a TTM, to an upward-looking acoustic Doppler profiler mounted on the TTM anchor. This comparison shows excellent agreement between the ADV and Doppler profiler measurements of mean velocity. The  $\bar{u}$ ,  $\bar{v}$ , and  $\bar{w}$  components have a root-mean-square error of 0.05, 0.13, and 0.03 m/s, respectively. Although it is important to note that there is some discrepancy between ADP- and ADV-measured velocities (especially in  $\bar{v}$ , which is most likely due to incomplete motion correction), the agreement between the magnitude and direction of these independent velocity measurements indicates that moored ADV-IMUs provide a reliable estimate of mean velocity in the Earth’s reference frame.

### *b. TTM spectra*

As discussed in detail in Part 1, the mooring motion of the TTM,  $S\{\vec{u}_h\}$ , has a peak at 0.1 to 0.2 Hz from swaying of the mooring that is most likely driven by eddy shedding from the spherical buoy (Figure 8, red lines). There is also higher-frequency broadband motion that is associated with fluttering of the strongback fin around the mooring line. Both of these motions are especially energetic in the  $v$ -component spectra because this is the direction in which the TTM mooring system is most unstable. As is expected from fluid-structure interaction theory, the amplitude of these motions increases with increasing mean velocity (Morison et al. 1950).

The mooring motion contaminates the uncorrected ADV measurements of velocity,  $S\{\vec{u}_m\}$ , whenever the amplitude of the motion is similar to or greater than the amplitude of the turbulence. Fortunately, much of this motion can be removed using the IMU’s motion signals as detailed in Section 3. Lacking an independent measurement of turbulence velocity at this site, we

interpret the agreement of these spectra with turbulence theory as evidence that motion correction has improved the velocity measurements. In particular, at high frequencies ( $f > 0.3$  Hz) for each mean-flow speed, the spectra decay with a  $f^{-5/3}$  slope and have equal amplitude across the velocity components. These results are consistent with Kolmogorov’s (1941) theory of isotropic turbulence, and are consistent with spectral shapes of earlier measurements of turbulence in energetic tidal channels from stationary platforms (Walter et al. 2011; Thomson et al. 2012; McMillan et al. 2016).

For  $|\vec{u}| > 1.0$ , motion correction modifies the  $u$  and  $v$  component spectra at frequencies as high as 3 Hz. This outcome indicates that in order for motion correction to be effective, synchronization between the ADV and IMU needs to be within 1/3 s or better. This suggests that asynchronous approaches to motion correction may be challenging, especially considering that the clock drift of some instrumentation can be as high as a few seconds per day. By integrating the IMU data into the ADV data stream, the Nortek ADV-IMU achieves a synchronization to within 1e-2 s.

At low frequencies the spectra tend to become roughly constant (especially at higher flow speeds), which is also consistent with previous works. Note that the very low magnitude of  $S\{\vec{u}_h\}$  at low frequencies is partially a result of filtering the IMU’s accelerometer signal when calculating  $\vec{u}_a$ . The true low-frequency spectrum of ADV head motion is unknown (indicated using a dashed line below  $f_a$ ). A comparison of  $S\{\vec{u}\}$  measured by the TTM to that measured by the ADP—during the June 2012 deployment—reveals agreement at low frequencies (not shown). This finding suggests that the assumption that  $\vec{u}_{low} = 0$  at these frequencies and at this site for this platform is justified—even if  $S\{\vec{u}_h\}$  is not as low as indicated in Figure 8.

As successful as motion correction is, some of the motion contamination persists in  $S\{\vec{u}\}$ . This is most notable in  $S\{v\}$  at the highest flow speeds ( $> 2.0$  m/s): a peak at 0.15 Hz is an order of magnitude larger than a spectral fit to the other frequencies would indicate. This persistent motion

contamination is evident to a lesser degree in  $S\{u\}$  for  $|u| > 2$  m/s, and in  $S\{v\}$  at lower flow speeds.  $S\{w\}$  appears to have no persistent motion contamination because the amplitude of the motion in this direction is much lower than for the other two components. For these measurements,  $S\{w_h\}$  is so low that  $w$ -component motion correction makes only a minor correction to the spectra.

The amplitude of the persistent motion contamination peaks in  $S\{v\}$  at 0.15 Hz is a factor of 5 to 10 times smaller than the amplitude of the ADV head motion itself. This observation suggests that the Microstrain IMU can be used to effectively correct mooring motion at 0.15 Hz when the amplitude of that motion is less than 5 times the amplitude of the real turbulence spectrum. As a result, we have chosen a value of 3 as a conservative estimate of the motion correction's effectiveness.

In addition to the primary benefit of correcting for mooring motion, the IMU measurements can also be used to identify and screen out persistent motion contamination. For example, one of the most common uses of turbulence spectra is for the calculation of  $\varepsilon$  and  $\text{tke}$ . For these purposes, and based on the relative amplitudes of the 0.15-Hz peaks, we assume that persistent motion contamination is likely, where  $S\{\vec{u}_h\}/S\{\vec{u}\} > 3$ , and thereby exclude these regions from spectral fits.

In the present case, for the  $u$  and  $w$  spectra, this criteria only excludes a narrow range of frequencies at the 0.15-Hz motion peak for some cases. This criteria is more restrictive of the  $v$ -component spectra at high frequencies for  $\bar{U} > 1.0$  m/s, but this may be acceptable because the amplitude of  $S\{v\}$  at these frequencies—i.e., in the isotropic inertial subrange—should be equal to that of  $S\{u\}$  and  $S\{w\}$  (Kolmogorov 1941).

Agreement of the  $v$ -component spectral amplitude with that of  $u$  and  $w$  at frequencies  $> 0.3$  Hz indicates that motion correction is effective at those frequencies even when  $S\{\vec{u}_h\}/S\{\vec{u}\} \gtrsim 3$ . This outcome suggests that our screening threshold is excessively conservative at those frequencies,



and that a more precise screening threshold may be frequency dependent. For example, it might take into account the  $f^3$  character of the noise in  $S\{\vec{u}_a\}$  (Figure 6). For the purpose of this work, the  $S\{\vec{u}_h\}/S\{\vec{u}\} < 3$  threshold for spectral fits is sufficient, and detailed characterization of the IMU’s motion- and frequency-dependent noise level is left for future work.

### c. *StableMoor Spectra*

The spectra of the StableMoor motion has a broader peak with a maximum amplitude that is approximately half the frequency of the TTM spectral peak (Figure 9). The motion of this platform also does not have high-frequency “subpeaks” or other high-frequency broadbanded excitation (Part 1). These characteristics of the motion are most likely due to the more massive and hydrodynamically streamlined properties of the platform.

Like the TTM, the motion-corrected spectra from the StableMoor buoy are consistent with turbulence theory and previous observations. Most importantly, there is an improvement in the quality of the motion-corrected spectra compared to the TTM. In particular, the persistent motion contamination peaks are completely removed. That is, this measurement system provides an accurate estimate of the turbulence spectra at this location from low frequencies to more than 1 Hz—well into the inertial subrange—for all three components of velocity.

Note that this level of accuracy cannot be obtained without the independent estimate of  $\vec{u}_{low}$ . If we assume that  $\vec{u}_{low} = 0$ , a similar plot to Figure 9 (not shown) reveals persistent motion-contamination peaks and troughs in the  $u$  and  $v$  spectra regardless of the choice of  $f_a$ . This assumption indicates that the low-frequency motion of the StableMoor buoy is below a threshold in which the IMU’s signal-to-noise ratio is high enough to resolve its motion. In other words, compared to the TTM, the StableMoor platform provides a more accurate measurement of turbulence

when it includes an independent measure of  $\vec{u}_{\text{low}}$  (here a bottom-tracking ADCP), but it does no better—and perhaps worse—when it does not.

#### *d. Torpedo spectra*

The  $u$  and  $v$  motion of the turbulence torpedo is broadband and the  $w$  motion has a narrow peak at 0.3 Hz (Figure 10). Because  $\vec{u}_h$  is estimated using  $f_a = 0.0333 \text{ Hz}$  and assuming  $\vec{u}_{\text{low}} = 0$ , its spectra rolls off quickly below  $f_a$ . Motion correction of the torpedo data appears to effectively remove a motion peak from  $S\{w\}$  at 0.3 Hz, and straightens out  $S\{v\}$  between 0.04 and 0.6 Hz.  $S\{u\}$  is mostly unaffected by motion at these frequencies, because the torpedo motion is smaller than the turbulence in this direction. At frequencies below  $f_a$ ,  $S\{u\}$  and  $S\{v\}$  increase dramatically. This increase suggests that unresolved, low-frequency motion of the torpedo is contaminating the velocity measurements at these frequencies. It may be possible to correct for some of this contamination using a measurement of the ship’s motion as a proxy for the torpedo’s low-frequency motion, but this has not been done. Still, above  $f_a$ , the torpedo appears to provide a reliable estimate of spectral amplitude in the inertial subrange and can therefore be used to estimate  $\epsilon$ . Considering the simplicity of the platform, it may be a useful option for quantifying this turbulence statistic in a variety of scenarios. Further, if a GPS is positioned above it, it may be capable of providing even more.

#### *e. Cross Spectra*

Cross-spectra indicate the correlation between different velocity components as a function of frequency, and their integrals are the Reynold’s stresses. Head motion cross-spectra,  $C\{\vec{u}_h\}$  (Figure 11, red), and uncorrected velocity cross-spectra,  $C\{\vec{u}_m\}$  (black), from TTM measurements have large peaks at the same frequency ( 0.15 Hz) as peaks in auto-spectra (Figure 8). This indicates

392 that mooring motion contaminates the uncorrected cross-spectral velocity measurements, and that  
393 Reynold's stress estimates based on uncorrected velocity measurements will be contaminated by  
394 mooring motion. This makes sense because mooring swaying in a direction not aligned with one  
395 of the major principal axes will, for example, introduce spurious cross-spectra and contaminate  
396 the Reynold's stress.

397 Fortunately, motion corrected velocity cross-spectra,  $C\{\vec{u}\}$  (blue), have reduced spectral ampli-  
398 tudes at these frequencies (reduced peaks), which indicates that motion correction reduces motion  
399 contamination to produce more reliable estimates of velocity cross spectra and Reynold's stresses  
400 (Figure 11). In particular, the uncertainty in  $f \cdot C\{\vec{u}\}$  (indicated by the blue shading), is signifi-  
401 cantly smaller than the mean values of  $C\{\vec{u}_h\}$  and  $C\{\vec{u}_m\}$  at the frequencies of maximum motion  
402 (0.15 Hz). This indicates that even the individual estimates of  $C\{\vec{u}\}$  have reduced peaks at these  
403 frequencies, not just the mean.

404 These results indicate that motion-corrected TTM velocity measurements can be used to obtain  
405 reliable estimates of turbulence Reynold's stresses, which are the integral of the cross spectra.  
406 Without motion correction, Reynold's stress estimates would be contaminated by the large peaks  
407 in the cross spectra that are caused by the swaying and fluttering motion of the TTM vane.

408 A similar investigation of StableMoor cross spectra (not shown) indicates that cross-spectral  
409 motion contamination is at a much lower amplitude than for the TTM. The low-frequency ( $< 0.3$   
410 Hz) "swimming" motion of that platform produces a minimal cross-spectral signal, and the relative  
411 large mass of the platform minimizes the kinds of higher-frequency swaying and fluttering that  
412 creates large values of cross-spectral head motion. Thus, the StableMoor platform also produces  
413 reliable estimates of Reynold's stresses, which are presumed to be improved by motion correction.

## 5. Discussion

The previous section presented a comparison of  $\vec{u}$  measured by a TTM-mounted ADV to measurements from a co-located ADP. This comparison demonstrated that the IMU provides a reliable estimate of the ADV’s orientation and that this can be utilized to estimate mean velocity in the Earth’s reference frame. Turbulence velocity estimates from the same ADP are also in agreement with low-frequency TTM turbulence estimates (not shown), but the ADP does not resolve turbulence at the scales where motion contamination is strongest (0.1 to 1.0 Hz).

Ideally, moored motion-corrected turbulence velocity measurements would be validated against simultaneous independent validated measurements of turbulence velocity at the same scales and exact time and location. Accomplishing this, however, involves significant technical challenges that are not easily overcome—most notably the difficulty of measuring turbulence at the same point as the moving ADV. A slightly less ideal but much more realistic confirmation of the methodology might involve comparing the statistics of moored turbulence measurements to those from a nearby fixed platform, or a fixed platform placed at the same location at a different time (e.g., the “TTT” platform described in Thomson et al. 2012). Unfortunately, to our knowledge, these measurements have not yet been made.

Lacking a relevant, fixed, independent turbulence measurement to compare to it is instructive to demonstrate the degree to which the moored measurements are consistent with turbulence theory and other turbulence measurements in similar flow environments. The previous section showed that the shape of the turbulence velocity spectra from moored ADVs is consistent with Kolmogorov’s theory of locally isotropic turbulence, which has been observed consistently in turbulence measurements for decades (Kolmogorov 1941; Grant et al. 1962; McMillan et al. 2016). In particular, we observed an isotropic subrange—an  $f^{-5/3}$  spectral slope and equal amplitude

spectra between components—that is driven by anisotropic turbulence at longer timescales (Figures 8, 9, 10). This finding is interpreted as the first indication that the measurement systems presented are capable of accurately resolving turbulence. The degree to which uncorrected spectra were corrected toward this theoretical and observationally confirmed shape is interpreted as a measure of the improvement of the spectral estimates by motion correction.

Figure 12 presents a time series of the mean velocity (A) and several turbulence statistics that were measured during the June 2014 TTM deployment. This figure shows the evolution of the flow through Admiralty Inlet during 1.5 tidal cycles. The tke (B), Reynold’s stresses (C), dissipation, and one component of turbulence production (D) grow and strengthen with ebb or flood then subside during slack tide. This component of turbulence production is:

$$P_{uz} = \frac{\partial \bar{u}}{\partial z} \overline{uw} \quad . \quad (4)$$

Where  $\partial \bar{u} / \partial z$  is computed from the two ADVs on the TTM. The highest values of  $\varepsilon$  and  $P_{uz}$  occur at the peak of the ebb or flood, which is in agreement with other measurements in tidal channels. The agreement of the magnitude of  $P_{uz}$  with  $\varepsilon$  at those times suggests a local production-dissipation balance that is often observed in tidally forced channels (Trowbridge et al. 1999; Stacey et al. 1999b; McMillan et al. 2016). At other times, the value of  $P_{uz}$  is insufficient to balance  $\varepsilon$  or is negative.

Inspection of the negative  $P_{uz}$  values reveals that most of them are caused by a reversed sign of  $\overline{uw}$  rather than a reversed sign of  $\partial u / \partial z$  (i.e., when compared to the sign of  $u$ ). This finding suggests that uncertainty in  $\overline{uw}$  may be contributing to discrepancies between  $P_{uz}$  and  $\varepsilon$ . Furthermore, considering the complex nature of the shoreline near this site (i.e., the headland), it is not surprising that  $P_{uz}$  does not balance  $\varepsilon$  perfectly. Other terms of the tke equation are likely to be important, such as other components of production, advection terms, or turbulent transport terms. The fact

that these two terms are in near balance as often as they are is a strong indication that bottom boundary layer physics are important to the dynamics at this site.

Figure 13 compares individual values of  $P_{uz}$  with  $\varepsilon$  directly. Given the assumptions implicit in this comparison and the discussion above, the agreement between  $P_{uz}$  and  $\varepsilon$  is an encouraging result that suggests the turbulent boundary layer reaches the depth of these measurements (10 m) during the highest flow speeds. This result is further supported by a comparison of  $\bar{U}$  with  $\varepsilon$  (Figure 14). Here we see a  $\varepsilon \propto \bar{U}^3$  dependence that is again suggestive of bottom boundary layer physics (Trowbridge 1992; Nash et al. 2009). At lower flow speeds,  $\varepsilon$  deviates from this relationship, which suggests that the boundary layer is no longer the dominant physical process at the depth of these measurements.

## 6. Conclusion

This work presents a methodology for measuring turbulence from moored ADV-IMUs and demonstrates that motion correction reduces mooring motion-contamination. Comparison of spectra of ADV head motion,  $S\{\vec{u}_h\}$ , to that of motion-corrected,  $S\{\vec{u}\}$ , and uncorrected spectra,  $S\{\vec{u}_m\}$ , reveals that motion correction improves spectral estimates of moored ADV measurements. In particular, we found that motion-corrected spectra have spectral shapes that are similar to previous measurements of tidal-channel turbulence and have a  $f^{-5/3}$  spectral slope at high frequencies. This finding suggests that the motion-corrected spectra resolve the inertial subrange predicted by Kolmogorov’s theory of locally isotropic turbulence.

Motion correction reduces motion contamination for all platforms we presented but it does not necessarily remove it completely. This outcome seems to depend on the relative amplitude of platform motion compared to the underlying turbulence being measured. The most notable example of this is from the TTM, which has a large “swaying” peak at 0.1 Hz. Where this peak

482 is very large—especially in the  $v$  component—it is not reduced to a level that is consistent with  
483 earlier measurements of tidal-channel turbulence—i.e., there is no smooth roll-off between the  
484 low-frequency energy-containing scales and the  $f^{-5/3}$  inertial subrange.

485 This inconsistency indicates that turbulence measurements from moored, motion-corrected  
486 ADV-IMUs must be interpreted with care. An inspection of spectra presented here suggests that  
487 excluding spectral regions where  $S\{\vec{u}_h\}/S\{\vec{u}\} > 3$  removes persistent-motion contamination peaks  
488 while still preserving spectral regions where motion correction is effective. Using this criteria, it  
489 is then possible to produce spectral fits that exclude persistent-motion contamination, and provide  
490 reliable estimates of turbulence quantities of interest (e.g.,  $\varepsilon$  and  $\text{tke}$ ).

491 We have also shown that motion correction reduces motion contamination in cross spectra. This  
492 finding is important because it suggests that moored ADV-IMU measurements may be used to  
493 produce reliable estimates of Reynolds stresses. We utilized these stress estimates and vertical  
494 shear estimates, both from the TTM, to estimate  $P_{uz}$ .

495 Finally, we have shown that  $\varepsilon$  estimates based on motion-corrected spectra scale with the  $U^3$ , and  
496 balance  $P_{uz}$  estimates during ebb and flood. Together, these results indicate that bottom boundary  
497 layer physics are a dominant process at this site, and that the boundary layer reaches the height  
498 of the ADV-IMUs (10 m) during ebb and flood. The degree of agreement between  $P_{uz}$  and  $\varepsilon$  also  
499 serves as an indicator of the self-consistency of moored ADV-IMU turbulence measurements.

500 *Acknowledgments.* Many thanks to Joe Talbert, Alex DeKlerk, Captain Andy Reay-Ellers, Jen-  
501 nifer Rinker, Maricarmen Guerra, and Eric Nelson in assisting with data collection. The authors  
502 are also grateful to James VanZwieten, Matthew Egeland and Marshall Richmond for discussion  
503 on the details of this work.

504 Thanks to the open-source software community for the tools used in this work, especially the  
505 developers of L<sup>A</sup>T<sub>E</sub>X, Python, NumPy, Matplotlib, git, and GNU emacs.

506 This work was supported by the U.S. Department of Energy under Contract No. DE-AC36-  
507 08GO28308 with the National Renewable Energy Laboratory. Funding for the work was provided  
508 by the DOE Office of Energy Efficiency and Renewable Energy, Wind and Water Power Technolo-  
509 gies Office.

510 The U.S. Government retains and the publisher, by accepting the article for publication, ac-  
511 knowledges that the U.S. Government retains a nonexclusive, paid-up, irrevocable, worldwide  
512 license to publish or reproduce the published form of this work, or allow others to do so, for U.S.  
513 Government purposes.



## References

- Afgan, I., J. McNaughton, S. Rolfo, D. Apsley, T. Stallard, and P. Stansby, 2013: Turbulent flow and loading on a tidal stream turbine by les and rans. *International Journal of Heat and Fluid Flow*, **43**, 96–108.
- Alexander, S. R., and P. E. Hamlington, 2015: Analysis of turbulent bending moments in tidal current boundary layers. *Journal of Renewable and Sustainable Energy*, **7** (6), 063 118.
- Alford, M. H., 2010: Sustained, full-water-column observations of internal waves and mixing near mendocino escarpment. *Journal of Physical Oceanography*, **40** (12), 2643–2660, doi:10.1175/2010JPO4502.1.
- Axford, D., 1968: On the accuracy of wind measurements using an inertial platform in an aircraft, and an example of a measurement of the vertical mesostructure of the atmosphere. *Journal of Applied Meteorology*, **7** (4), 645–666.
- Barshan, B., and H. F. Durrant-Whyte, 1995: Inertial navigation systems for mobile robots. *IEEE Transactions on Robotics and Automation*, **11** (3), 328–342.
- Bevly, D. M., 2004: Global positioning system (gps): A low-cost velocity sensor for correcting inertial sensor errors on ground vehicles. *Journal of dynamic systems, measurement, and control*, **126** (2), 255–264.
- Cartwright, G. M., C. T. Friedrichs, P. J. Dickhudt, T. Gass, and F. H. Farmer, 2009: Using the acoustic doppler velocimeter (adv) in the mudbed real-time observing system. *Marine Technology for Our Future: Global and Local Challenges*.
- Doherty, K., D. Frye, S. Liberatore, and J. Toole, 1999: A moored profiling instrument\*. *Journal of Atmospheric and Oceanic Technology*, **16** (11), 1816–1829.

536 Edson, J. B., A. A. Hinton, K. E. Prada, J. E. Hare, and C. W. Fairall, 1998: Direct covariance  
 537 flux estimates from mobile platforms at sea\*. *Journal of Atmospheric and Oceanic Technology*,  
 538 **15** (2), 547–562, doi:10.1175/1520-0426(1998)015<0547:DCFEFM>2.0.CO;2.

539 Egeland, M. N., 2014: Spectral evaluation of motion compensated ADV systems for ocean turbu-  
 540 lence measurements. Ph.D. thesis, Florida Atlantic University.

541 Fer, I., and M. B. Paskyabi, 2014: Autonomous ocean turbulence measurements using shear probes  
 542 on a moored instrument. *Journal of Atmospheric and Oceanic Technology*, **31** (2), 474–490, doi:  
 543 10.1175/JTECH-D-13-00096.1.

544 Finlayson, D., 2005: Combined bathymetry and topography of the Puget Lowlands, Washington  
 545 state. URL <http://www.ocean.washington.edu/data/pugetsound/>.

546 Geyer, R. W., M. E. Scully, and D. K. Ralston, 2008: Quantifying vertical mixing in estuaries.  
 547 *Environmental Fluid Mechanics*, **8**, 495–509, doi:10.1007/s10652-008-9107-2.

548 Goodman, L., E. R. Levine, and R. G. Lueck, 2006: On measuring the terms of the turbulent  
 549 kinetic energy budget from an auv. *Journal of Atmospheric and Oceanic Technology*, **23** (7),  
 550 977–990, doi:10.1175/JTECH1889.1.

551 Grant, H. L., R. W. Stewart, and A. Moilliet, 1962: Turbulence spectra from a tidal channel.  
 552 *Journal of Fluid Mechanics*, **12**, 241–263.

553 Gulmammadov, F., 2009: Analysis, modeling and compensation of bias drift in mems inertial  
 554 sensors. *Recent Advances in Space Technologies, 2009. RAST'09. 4th International Conference*  
 555 *on*, IEEE, 591–596.

556 Gunawan, B., V. S. Neary, and J. Colby, 2014: Tidal energy site resource assessment in the East  
557 River tidal strait, near Roosevelt Island, New York, NY (USA). *Renewable Energy*, **71**, 509–  
558 517, doi:10.1016/j.renene.2014.06.002.

559 Hand, M. M., N. D. Kelley, and M. J. Balas, 2003: Identification of wind turbine response to  
560 turbulent inflow structures. Tech. Rep. NREL/CP-500-33465, National Renewable Energy Lab-  
561 oratory.

562 Harding, S., L. Kilcher, and J. Thomson, 2017: Turbulence measurements from compliant moor-  
563 ings - part 1: Motion characterization, in review.

564 Kelley, N. D., B. J. Jonkman, G. N. Scott, J. T. Bialasiewicz, and L. S. Redmond, 2005: The impact  
565 of coherent turbulence on wind turbine aeroelastic response and its simulation. *WindPower*,  
566 Denver, Colorado, NREL/CP-500-38074, may 15-18.

567 Kilcher, L., J. Thomson, J. Talbert, and A. DeKlerk, 2016: Measuring turbulence from moored  
568 acoustic Doppler velocimeters: A manual to quantifying inflow at tidal energy sites. 9 62979,  
569 National Renewable Energy Laboratory. URL [www.nrel.gov/docs/fy16osti/62979.pdf](http://www.nrel.gov/docs/fy16osti/62979.pdf).

570 Kim, S. C., C. T. Friedrichs, J. P.-Y. Maa, and L. D. Wright, 2000: Estimating bottom stress in  
571 tidal boundary layer from acoustic doppler velocimeter data. *Journal of Hydraulic Engineering*,  
572 399–406.

573 Kolmogorov, A. N., 1941: Dissipation of energy in the locally isotropic turbulence. *Dokl. Akad.*  
574 *Nauk SSSR*, **32** (1), 16–18, URL <http://www.jstor.org/stable/51981>.

575 Kraus, C., A. Lohrmann, and R. Cabrera, 1994: A new acoustic meter for measuring 3d laboratory  
576 flows. *Journal of Hydraulic Engineering*, **120**, 406–412.

577 Lohrmann, A., R. Cabrera, G. Gelfenbaum, and J. Haines, 1995: Direct measurements of reynolds  
578 stress with an acoustic doppler velocimeter. *Current Measurement, 1995., Proceedings of the*  
579 *IEEE Fifth Working Conference on*, 205–210, doi:10.1109/CCM.1995.516175.

580 Lorke, A., 2007: Boundary mixing in the thermocline of a large lake. *Journal of Geophysical*  
581 *Research: Oceans*, **112 (C9)**, n/a–n/a, doi:10.1029/2006JC004008, c09019.

582 Lueck, R. G., and D. Huang, 1999: Dissipation measurement with a moored instrument in a swift  
583 tidal channel. *Journal of atmospheric and oceanic technology*, **16**, 1499–1505.

584 Lumley, J., and E. Terray, 1983: Kinematics of turbulence convected by a random wave field.  
585 *Journal of Physical Oceanography*, **13 (11)**, 2000–2007.

586 McCaffrey, K., B. Fox-Kemper, P. E. Hamlington, and J. Thomson, 2015: Characterization of  
587 turbulence anisotropy, coherence, and intermittency at a prospective tidal energy site: Observa-  
588 tional data analysis. *Renewable Energy*, **76**, 441–453.

589 McMillan, J. M., A. E. Hay, R. G. Lueck, and F. Wolk, 2016: Rates of dissipation of turbulent  
590 kinetic energy in a high reynolds number tidal channel. *Journal of Atmospheric and Oceanic*  
591 *Technology*, **33 (4)**, 817–837, doi:10.1175/JTECH-D-15-0167.1.

592 MicroStrain, I., 2010: Technical note: Coning and sculling. Tech. Rep. I0019, MicroStrain. URL  
593 [http://files.microstrain.com/TN-I0019\\_3DM-GX3-25\\_\\_Coning\\_And\\_Sculling.pdf](http://files.microstrain.com/TN-I0019_3DM-GX3-25__Coning_And_Sculling.pdf).

594 MicroStrain, I., 2012: *3DM-GX3-15,-25 MIP Data Communications Protocol*. URL [http:](http://files.microstrain.com/3DM-GX3-15-25-MIP-Data-Communications-Protocol.pdf)  
595 [//files.microstrain.com/3DM-GX3-15-25-MIP-Data-Communications-Protocol.pdf](http://files.microstrain.com/3DM-GX3-15-25-MIP-Data-Communications-Protocol.pdf), retrieved  
596 January 2014.

597 Miller, S. D., T. S. Hristov, J. B. Edson, and C. A. Friehe, 2008: Platform motion effects on  
 598 measurements of turbulence and air-sea exchange over the open ocean. *Journal of Atmospheric*  
 599 *and Oceanic Technology*, **25** (9), 1683–1694, doi:10.1175/2008JTECHO547.1.

600 Morison, J. R., J. W. Johnson, and S. A. Schaaf, 1950: The force exerted by surface waves on  
 601 piles. *Journal of Petroleum Technology*, **2** (05), 149–154.

602 Moum, J., and J. Nash, 2009: Mixing measurements on an equatorial ocean mooring. *Journal of*  
 603 *Atmospheric and Oceanic Technology*, **26** (2), 317–336.

604 Mücke, T., D. Kleinhans, and J. Peinke, 2011: Atmospheric turbulence and its influence on the  
 605 alternating loads on wind turbines. *Wind Energy*, **14**, 301–316.

606 Nash, J. D., L. F. Kilcher, and J. N. Moum, 2009: Structure and composition of a strongly  
 607 stratified, tidally pulsed river plume. *Journal of Geophysical Research*, **114**, C00B12, doi:  
 608 10.1029/2008JC005036.

609 Nash, J. D., E. Kunze, J. M. Toole, and R. W. Schmitt, 2004: Internal tide reflection and turbulent  
 610 mixing on the continental slope. *Journal of Physical Oceanography*, **34** (5), 1117–1134, doi:  
 611 10.1175/1520-0485(2004)034<1117:ITRATM>2.0.CO;2.

612 Nortek, 2005: *Vector Current Meter User Manual*. Vangkroken 2, NO-1351 RUD, Norway, h ed.

613 Paskyabi, M. B., and I. Fer, 2013: Turbulence measurements in shallow water from a subsurface  
 614 moored moving platform. *Energy Procedia*, **35**, 307 – 316, doi:10.1016/j.egypro.2013.07.183.

615 Perlin, A., and J. N. Moum, 2012: Comparison of thermal variance dissipation rates from moored  
 616 and profiling instruments at the equator. *Journal of Atmospheric and Oceanic Technology*.

617 Polagye, B., and J. Thomson, 2013: Tidal energy resource characterization: methodology and field  
618 study in admiralty inlet, Puget Sound, WA (USA). *Proceedings of the Institution of Mechanical*  
619 *Engineers, Part A: Journal of Power and Energy*, **227** (3), 352–367.

620 Rippeth, T. P., E. Williams, and J. H. Simpson, 2002: Reynolds stress and turbulent en-  
621 ergy production in a tidal channel. *Journal of Physical Oceanography*, **32**, 1242–1251, doi:  
622 10.1175/1520-0485(2002)032<1242:RSATEP>2.0.CO;2.

623 Sreenivasan, K. R., 1995: On the universality of the Kolmogorov constant. *Physics of Fluids*, **7**,  
624 2778–2784.

625 Stacey, M. T., S. G. Monismith, and J. R. Burau, 1999a: Measurements of reynolds stress  
626 profiles in unstratified tidal flow. *J. Geophys. Res.*, **104** (C5), 10 933–10 949, doi:10.1029/  
627 1998JC900095.

628 Stacey, M. T., S. G. Monismith, and J. R. Burau, 1999b: Observations of turbulence in a partially  
629 stratified estuary. *Journal of Physical Oceanography*, **29**, 1950–1970.

630 Thomson, J., B. Polagye, V. Durgesh, and M. Richmond, 2012: Measurements of turbulence at  
631 two tidal energy sites in Puget Sound, WA. *Journal of Oceanic Engineering*, **37** (3), 363–374,  
632 doi:10.1109/JOE.2012.2191656.

633 Trowbridge, J. H., 1992: A simple description of the deepening and structure of a stably stratified  
634 flow driven by a surface stress. *Journal of Geophysical Research*, **97**, 15 529–15 543.

635 Trowbridge, J. H., W. R. Geyer, M. M. Bowen, and A. J. I. Williams, 1999: Near-bottom turbu-  
636 lence measurements in a partially mixed estuary: turbulent energy balance, velocity structure  
637 and along-channel momentum balance. *Journal of Physical Oceanography*, **29**, 3056–3072.

638 van der Walt, S., S. C. Colbert, and G. Varoquaux, 2011: The numpy array: A structure for efficient  
639 numerical computation. *Computing in Science & Engineering*, **13**, 22–30, doi:10.1109/MCSE.  
640 2011.37.

641 VanZwieten, J. H., M. N. Egeland, K. D. von Ellenrieder, J. W. Lovenbury, and L. Kilcher, 2015:  
642 Experimental evaluation of motion compensated adv measurements for in-stream hydrokinetic  
643 applications. *Current, Waves and Turbulence Measurement (CWTM), 2015 IEEE/OES Eleventh*,  
644 1–8, doi:10.1109/CWTM.2015.7098119.

645 Voulgaris, G., and J. H. Trowbridge, 1998: Evaluation of the acoustic doppler velocimeter (adv)  
646 for turbulence measurements. *Journal of Atmospheric and Oceanic technology*, **15**, 272–289.

647 Walter, R. K., N. J. Nidzieko, and S. G. Monismith, 2011: Similarity scaling of turbulence spectra  
648 and cospectra in a shallow tidal flow. *Journal of Geophysical Research: Oceans*, **116 (C10)**.

649 Wiles, P. J., T. P. Rippeth, J. H. Simpson, and P. J. Hendricks, 2006: A novel technique for  
650 measuring the rate of turbulent dissipation in the marine environment. *Geophysical Research*  
651 *Letters*, **33**, 21 608.

652 Winkel, D., M. Gregg, and T. Sanford, 1996: Resolving oceanic shear and velocity with the multi-  
653 scale profiler. *Journal of Atmospheric and Oceanic Technology*, **13 (5)**, 1046–1072.

654 Wyngaard, J. C., L. Rockwell, and C. A. Friehe, 1985: Errors in the measurement of turbulence  
655 upstream of an axisymmetric body. *Journal of Atmospheric and Oceanic Technology*, **2 (4)**,  
656 605–614.

657 Zhang, Y., K. Streitlien, J. G. Bellingham, and A. B. Baggeroer, 2001: Acoustic doppler ve-  
658 locimeter flow measurement from an autonomous underwater vehicle with applications to deep

659 ocean convection. *Journal of Atmospheric and Oceanic Technology*, **18 (12)**, 2038–2051, doi:  
660 10.1175/1520-0426(2001)018<2038:ADVFMF>2.0.CO;2.



## LIST OF FIGURES

<b>Fig. 1.</b>	Bathymetry of Admiralty Inlet near Port Townsend, Washington, U.S.A. (Finlayson 2005). The red dot indicates the location of all measurements. The positive $u$ direction is the direction of ebb flow (thick arrow originating from red dot), and positive $v$ is away from Admiralty Head (smaller arrow).	35
<b>Fig. 2.</b>	Schematic diagram of the TTM; not to scale.	36
<b>Fig. 3.</b>	TTM components on the deck of the R/V Jack Robertson. The TTM includes two ADVs, with pressure cases mounted on opposite sides of the fin. The anchor stack includes a pop-up buoy for retrieval. The green arrow indicates the vector from the IMU to the ADV head (face of the transmit transducer).	37
<b>Fig. 4.</b>	Top: Alex DeKlerk checks to ensure that the StableMoor buoy is properly fastened to its anchor; the RDI workhorse ADCP can be seen in the rear instrument bay. A bridle is draped across the top of the buoy for deployment and recovery, and a small marker buoy fastened to the tail is useful during recovery. Bottom: a close-up of the StableMoor buoy with the ADV head and the top of its pressure case. The green arrow indicates the vector from the IMU to the ADV head.	38
<b>Fig. 5.</b>	The turbulence platform showing details of the ADV head and pressure case configuration. The green arrow indicates the vector from the IMU to the ADV head. The head cable was taped out of the way beneath the sounding weight tail fins shortly after taking this photo.	39
<b>Fig. 6.</b>	The spectral noise levels of rotational velocity ( $S\{\vec{n}_\omega\}$ , yellow) and translational velocity ( $S\{\vec{n}_a\}$ , black) estimated from an ADV-IMU resting motionless on a table. The $\vec{n}_a$ signals are unfiltered (black), and high-pass filtered at 30 s (magenta) and 5 s (green). Vertical dotted lines indicate the filter frequency. Blue lines are an estimate of $\vec{u}_{\text{low}}$ for the TTM. Solid and dashed lines indicate the horizontal and vertical components, respectively, of $S\{\vec{n}_a\}$ and $S\{\vec{u}_{\text{low}}\}$ . The horizontal and vertical Doppler noise levels of a Nortek Vector ADV configured to measure $\pm 4\text{m/s}$ are indicated by horizontal dash-dot and dotted lines, respectively. The shaded region indicates the range of $u$ spectral amplitudes presented herein ( $0.002 < \text{tke} < 0.03 \text{ m}^2/\text{s}^2$ , $1\text{e-}5 < \epsilon < 5\text{e-}4 \text{ W/kg}$ ).	40
<b>Fig. 7.</b>	Time series of tidal velocity at Admiralty Head from ADV-IMU measurements (black), and an acoustic Doppler profiler on the anchor (red). The profiler measurements—taken at the same depth as the ADV on the TTM—were contaminated by acoustic reflection from the strongback fin when it was inline with one of the profiler’s beams. Note that the vertical scale on the three axes vary by more than an order of magnitude; the small ticks in A and B are equivalent to the ticks in C.	41
<b>Fig. 8.</b>	Turbulence spectra from the June 2014 TTM deployment. Each column is for a range of streamwise velocity magnitudes (indicated at top). The rows are for each component of velocity (indicated to the lower right of the right column). The uncorrected spectra are in black and the corrected spectra are blue, and the spectra of ADV head motion, $\vec{u}_h$ , is red (also indicated in the legend). The vertical red dotted line indicates the filter frequency applied to the IMU accelerometers when estimating $\vec{u}_h$ ; below this frequency $S\{\vec{u}_h\}$ is plotted as a dashed line. Diagonal black dotted lines indicate a $f^{-5/3}$ slope. The number of spectral ensembles, $N$ , in each column is indicated in the top row.	42

703	<b>Fig. 9.</b>	Turbulence spectra from the StableMoor buoy. The axes layout and annotations are identical to Figure 8, except that $S\{\vec{u}_h\}$ is plotted as a solid line at all frequencies because it is measured at all frequencies.	43
704			
705			
706	<b>Fig. 10.</b>	Turbulence spectra from the turbulence torpedo during a 35-minute period when the mean velocity was 1.3 m/s. Annotations and line colors are identical to Figure 8.	44
707			
708	<b>Fig. 11.</b>	Variance preserving cross-spectra between components of $\vec{u}$ (blue), $\vec{u}_h$ (red), and $\vec{u}_m$ (black) from the June 2014 TTM deployment. The upper row is $f \cdot C\{u, v\}$ , the middle row is $f \cdot C\{u, w\}$ , and the bottom row is $f \cdot C\{v, w\}$ . Note that these cross-spectra are between components of a velocity vector (e.g., $\vec{u}$ ), not between different vectors (i.e., not between $\vec{u}$ and $\vec{u}_m$ ). The columns are for different ensemble-averages over distinct ranges of the stream-wise mean velocity magnitude (indicated above the top row). N is the number of spectral ensembles in each column. The light blue shading indicates one standard deviation of $f \cdot C\{\vec{u}\}$ . The number in the lower-right corner of each panel indicates the ensemble-averaged estimate of the Reynold's stress component (integral of the blue line) in units of $10^{-3} \text{ m}^2 \text{ s}^{-2}$ .	45
709			
710			
711			
712			
713			
714			
715			
716			
717			
718	<b>Fig. 12.</b>	Time series of mean velocities (A), turbulence energy and its components (B), Reynold's stresses (C), and turbulence dissipation rate (D) measured by the TTM during the June 2014 deployment. Shading indicates periods of ebb ( $\bar{u} > 1.0 \text{ ms}^{-1}$ , grey) and flood ( $\bar{u} < -1.0 \text{ ms}^{-1}$ , lighter grey).	46
719			
720			
721			
722	<b>Fig. 13.</b>	$P_{u\bar{z}}$ vs. $\varepsilon$ during the June 2014 TTM deployment for values of $ u  > 1 \text{ m/s}$ . Values of negative production are indicated as open circles.	47
723			
724	<b>Fig. 14.</b>	A log-log plot of $\varepsilon$ vs. $\bar{U}$ for the June 2014 TTM (diamonds) and May 2015 StableMoor (dots) deployments, during ebb (left) and flood (right). Black points are 5-minute averages. Green dots are mean values within speed bins of $0.2 \text{ m s}^{-1}$ width that have at least 10 points (50 minutes of data); their vertical bars are 95% bootstrap confidence intervals. The blue line shows a $U^3$ slope, wherein the proportionality constant (blue box) is calculated by taking the log-space mean of $\varepsilon/U^3$ .	48
725			
726			
727			
728			
729			

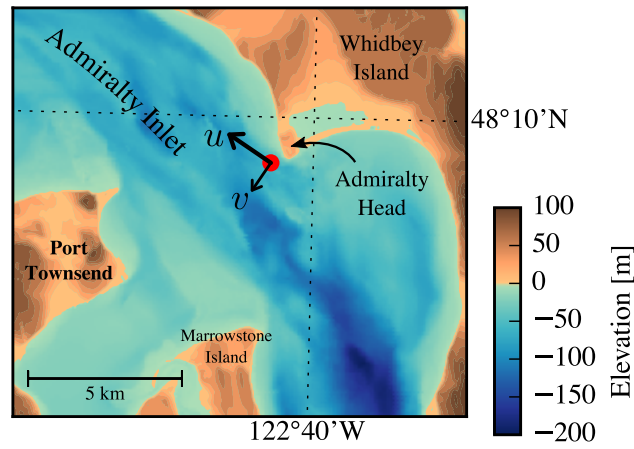


FIG. 1. Bathymetry of Admiralty Inlet near Port Townsend, Washington, U.S.A. (Finlayson 2005). The red dot indicates the location of all measurements. The positive  $u$  direction is the direction of ebb flow (thick arrow originating from red dot), and positive  $v$  is away from Admiralty Head (smaller arrow).

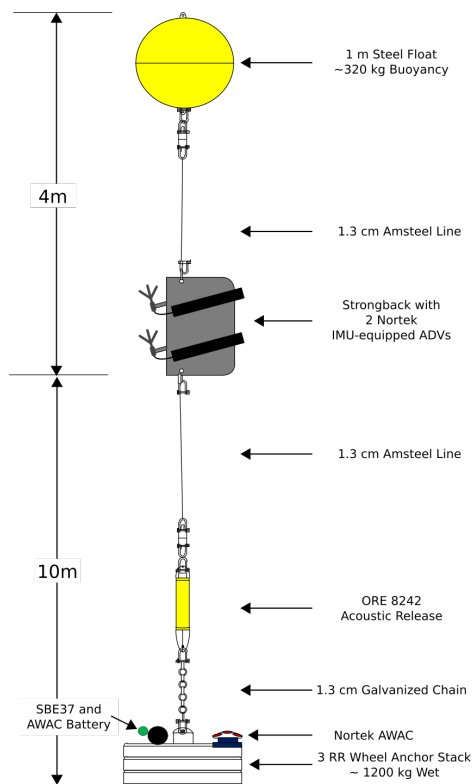


FIG. 2. Schematic diagram of the TTM; not to scale.



733 FIG. 3. TTM components on the deck of the R/V Jack Robertson. The TTM includes two ADVs, with  
 734 pressure cases mounted on opposite sides of the fin. The anchor stack includes a pop-up buoy for retrieval. The  
 735 green arrow indicates the vector from the IMU to the ADV head (face of the transmit transducer).



736 FIG. 4. Top: Alex DeKlerk checks to ensure that the StableMoor buoy is properly fastened to its anchor; the  
 737 RDI workhorse ADCP can be seen in the rear instrument bay. A bridle is draped across the top of the buoy  
 738 for deployment and recovery, and a small marker buoy fastened to the tail is useful during recovery. Bottom: a  
 739 close-up of the StableMoor buoy with the ADV head and the top of its pressure case. The green arrow indicates  
 740 the vector from the IMU to the ADV head.



741 FIG. 5. The turbulence platform showing details of the ADV head and pressure case configuration. The green  
742 arrow indicates the vector from the IMU to the ADV head. The head cable was taped out of the way beneath the  
743 sounding weight tail fins shortly after taking this photo.

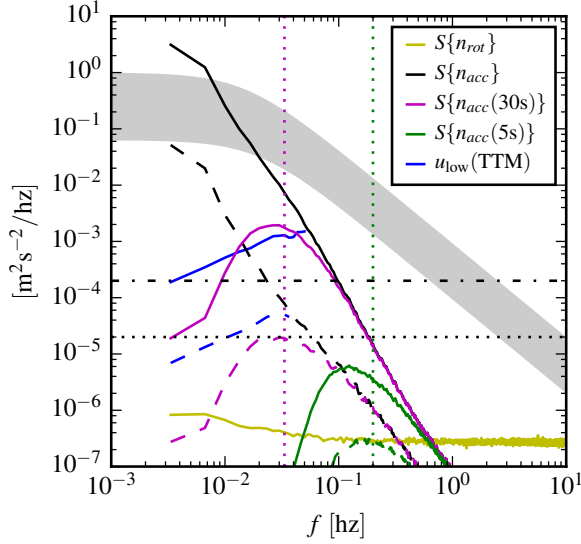


FIG. 6. The spectral noise levels of rotational velocity ( $S\{\vec{n}_\omega\}$ , yellow) and translational velocity ( $S\{\vec{n}_a\}$ , black) estimated from an ADV-IMU resting motionless on a table. The  $\vec{n}_a$  signals are unfiltered (black), and high-pass filtered at 30 s (magenta) and 5 s (green). Vertical dotted lines indicate the filter frequency. Blue lines are an estimate of  $\vec{u}_{\text{low}}$  for the TTM. Solid and dashed lines indicate the horizontal and vertical components, respectively, of  $S\{\vec{n}_a\}$  and  $S\{\vec{u}_{\text{low}}\}$ . The horizontal and vertical Doppler noise levels of a Nortek Vector ADV configured to measure  $\pm 4\text{m/s}$  are indicated by horizontal dash-dot and dotted lines, respectively. The shaded region indicates the range of  $u$  spectral amplitudes presented herein ( $0.002 < \text{tke} < 0.03 \text{ m}^2/\text{s}^2$ ,  $1\text{e-}5 < \varepsilon < 5\text{e-}4 \text{ W/kg}$ ).



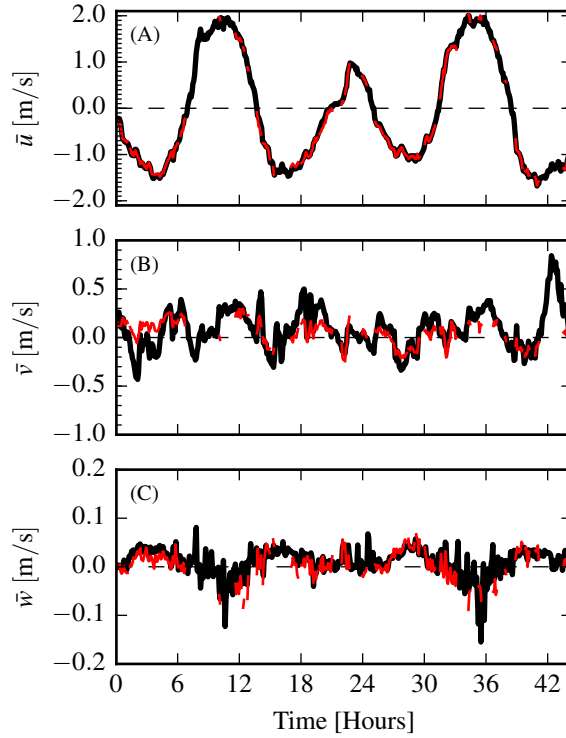


FIG. 7. Time series of tidal velocity at Admiralty Head from ADV-IMU measurements (black), and an acoustic Doppler profiler on the anchor (red). The profiler measurements—taken at the same depth as the ADV on the TTM—were contaminated by acoustic reflection from the strongback fin when it was inline with one of the profiler’s beams. Note that the vertical scale on the three axes vary by more than an order of magnitude; the small ticks in A and B are equivalent to the ticks in C.

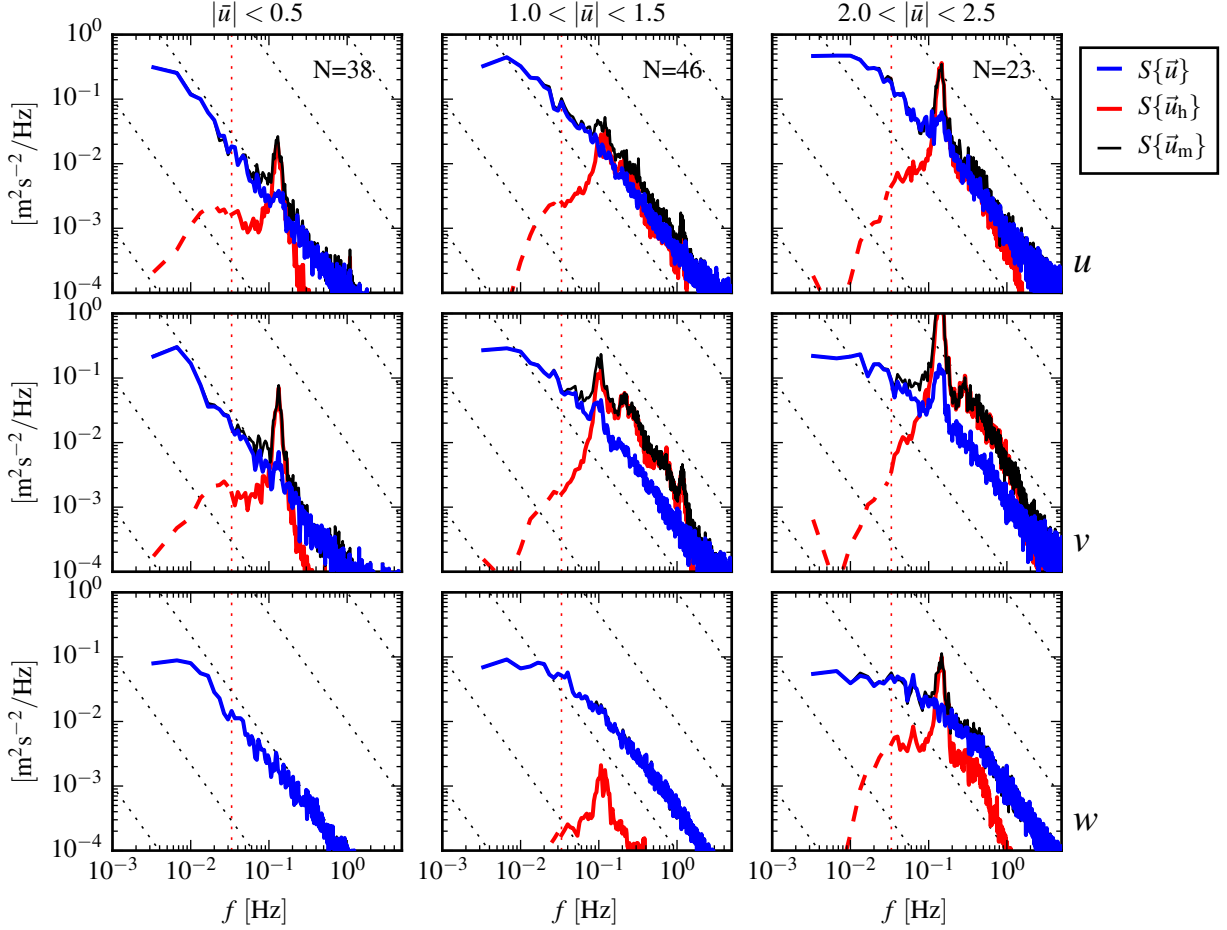


FIG. 8. Turbulence spectra from the June 2014 TTM deployment. Each column is for a range of streamwise  
 velocity magnitudes (indicated at top). The rows are for each component of velocity (indicated to the lower right  
 of the right column). The uncorrected spectra are in black and the corrected spectra are blue, and the spectra  
 of ADV head motion,  $\vec{u}_h$ , is red (also indicated in the legend). The vertical red dotted line indicates the filter  
 frequency applied to the IMU accelerometers when estimating  $\vec{u}_h$ ; below this frequency  $S\{\vec{u}_h\}$  is plotted as a  
 dashed line. Diagonal black dotted lines indicate a  $f^{-5/3}$  slope. The number of spectral ensembles,  $N$ , in each  
 column is indicated in the top row.

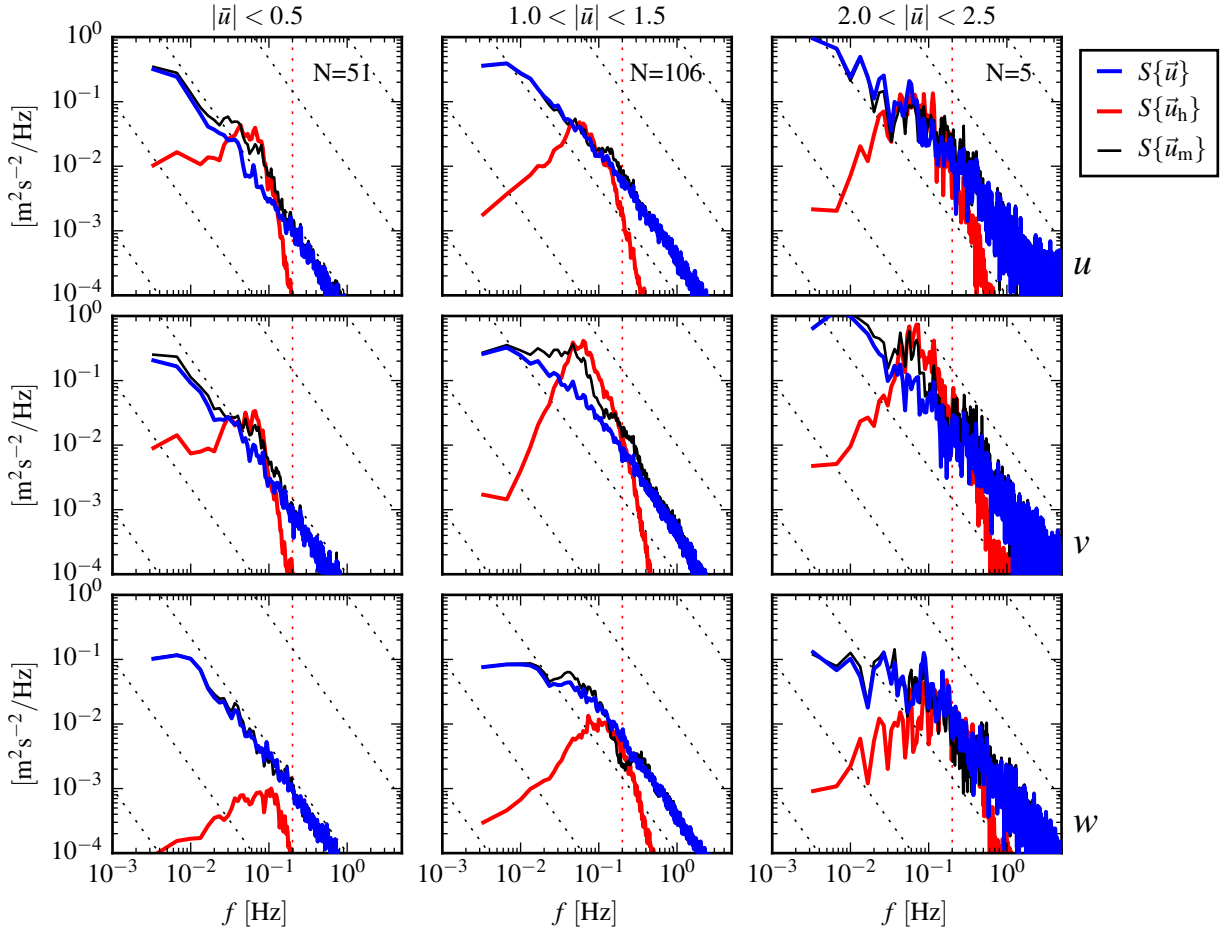


FIG. 9. Turbulence spectra from the StableMoor buoy. The axes layout and annotations are identical to Figure 8, except that  $S\{\vec{u}_h\}$  is plotted as a solid line at all frequencies because it is measured at all frequencies.

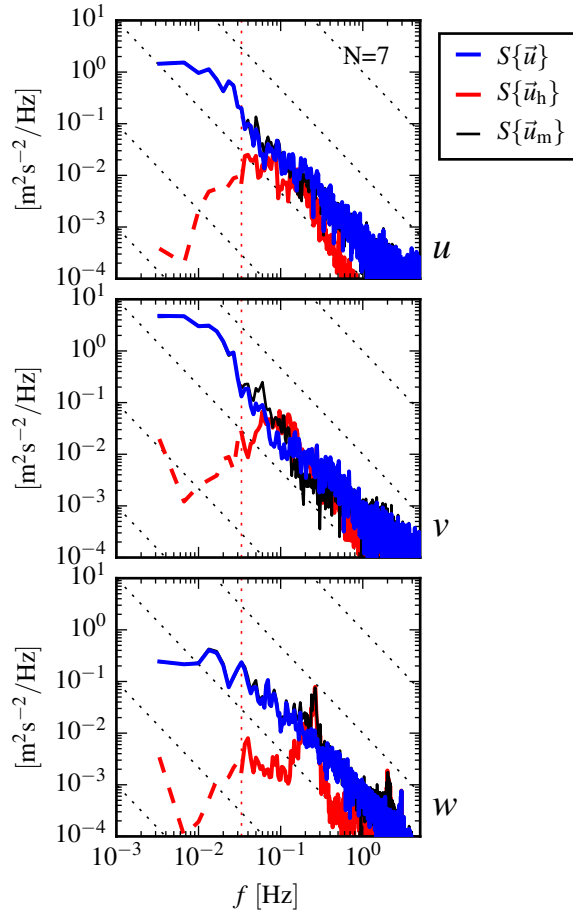


FIG. 10. Turbulence spectra from the turbulence torpedo during a 35-minute period when the mean velocity was 1.3 m/s. Annotations and line colors are identical to Figure 8.

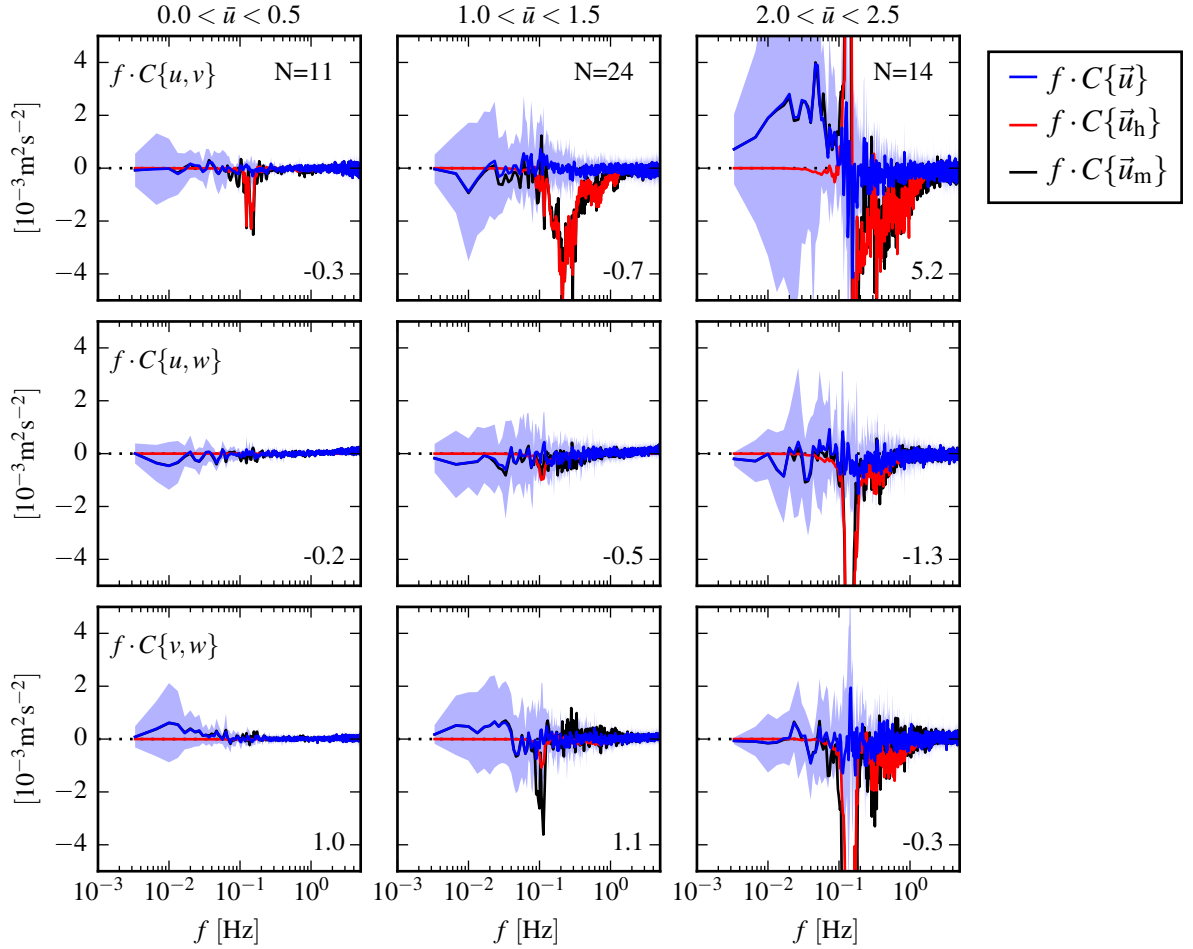


FIG. 11. Variance preserving cross-spectra between components of  $\vec{u}$  (blue),  $\vec{u}_h$  (red), and  $\vec{u}_m$  (black) from the June 2014 TTM deployment. The upper row is  $f \cdot C\{u, v\}$ , the middle row is  $f \cdot C\{u, w\}$ , and the bottom row is  $f \cdot C\{v, w\}$ . Note that these cross-spectra are between components of a velocity vector (e.g.,  $\vec{u}$ ), not between different vectors (i.e., not between  $\vec{u}$  and  $\vec{u}_m$ ). The columns are for different ensemble-averages over distinct ranges of the stream-wise mean velocity magnitude (indicated above the top row).  $N$  is the number of spectral ensembles in each column. The light blue shading indicates one standard deviation of  $f \cdot C\{\vec{u}\}$ . The number in the lower-right corner of each panel indicates the ensemble-averaged estimate of the Reynolds' stress component (integral of the blue line) in units of  $10^{-3} \text{ m}^2 \text{ s}^{-2}$ .

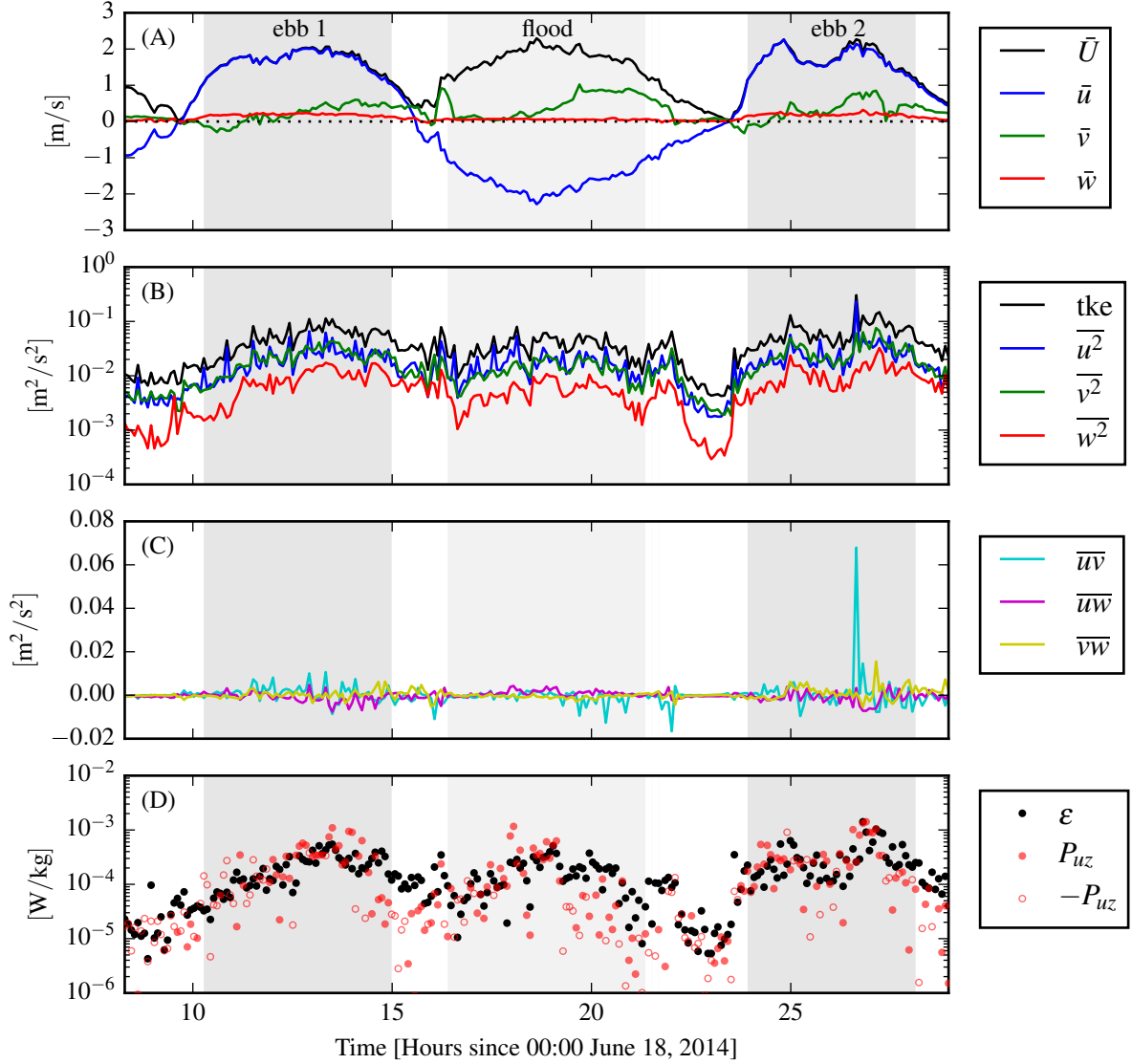


FIG. 12. Time series of mean velocities (A), turbulence energy and its components (B), Reynold's stresses (C), and turbulence dissipation rate (D) measured by the TTM during the June 2014 deployment. Shading indicates periods of ebb ( $\bar{u} > 1.0 \text{ ms}^{-1}$ , grey) and flood ( $\bar{u} < -1.0 \text{ ms}^{-1}$ , lighter grey).

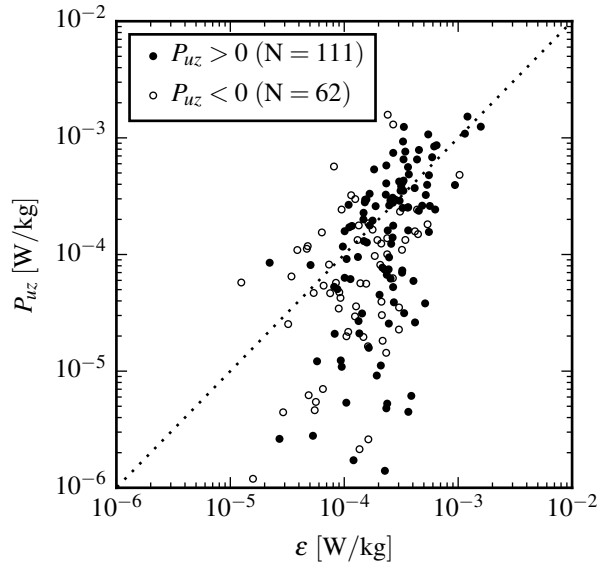


FIG. 13.  $P_{uz}$  vs.  $\varepsilon$  during the June 2014 TTM deployment for values of  $|u| > 1$  m/s. Values of negative production are indicated as open circles.

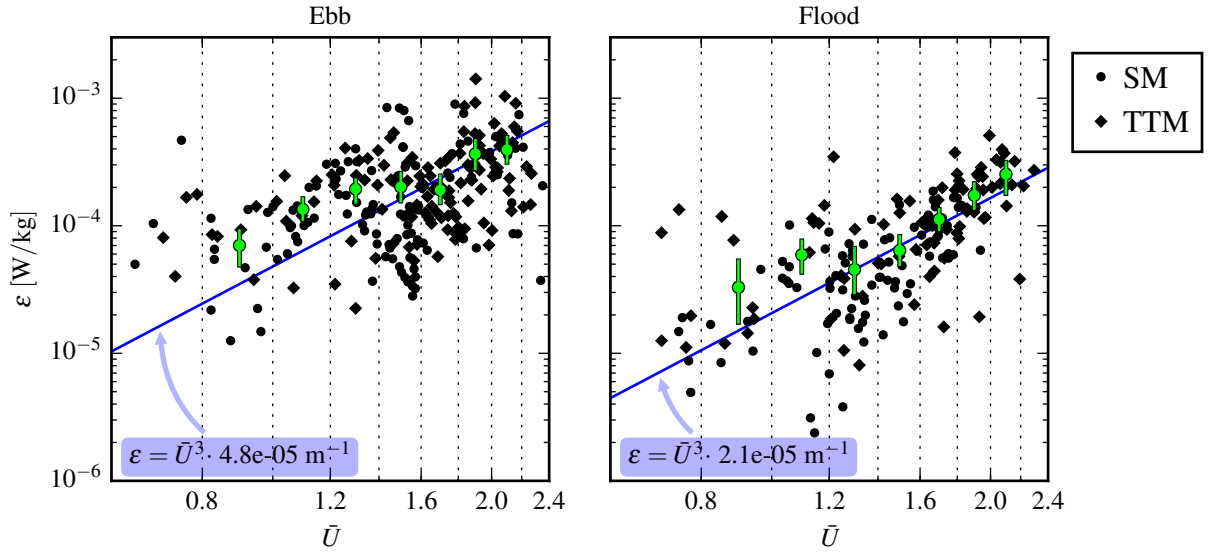


FIG. 14. A log-log plot of  $\epsilon$  vs.  $\bar{U}$  for the June 2014 TTM (diamonds) and May 2015 StableMoor (dots) deployments, during ebb (left) and flood (right). Black points are 5-minute averages. Green dots are mean values within speed bins of  $0.2 \text{ m s}^{-1}$  width that have at least 10 points (50 minutes of data); their vertical bars are 95% bootstrap confidence intervals. The blue line shows a  $U^3$  slope, wherein the proportionality constant (blue box) is calculated by taking the log-space mean of  $\epsilon/U^3$ .